Rev. Adv. Mater. Sci. 50 (2017) 76-87

MAGNETIC RESONANCE STUDY OF Co-DOPED ZnO NANOMATERIALS: A CASE OF HIGH DOPING

J. Typek[1], N. Guskos[1], G. Zolnierkiewicz[1], D. Sibera[2] and U. Narkiewicz[2]

[1]Institute of Physics, West Pomeranian University of Technology, Al. Piastow 48,70-311 Szczecin, Poland
[2]Institute of Chemical and Environment Engineering, West Pomeranian University of Technology, ul. Pulaskiego 10, 70-322 Szczecin, Poland

Received: December 31, 2016

Abstract. Magnetic resonance could be very useful technique in clarification of many unresolved problems in nano-magnetism of ZnO doped with transition metal ions, in particular with Co. In the first part of this paper a review of investigations of ZnO:Co nanomaterials using magnetic resonance techniques - electron paramagnetic resonance (EPR) and ferromagnetic resonance (FMR) - is presented. The preparation methods, the structural characteristics of the obtained materials and the main results of EPR/FMR studies are briefly described. In the second part the EPR/FMR investigations of a new series of $(CoO)_n(ZnO)_{1-n}$ nanocomposites (where the composition index n = 0.4, 0.5, 0.6 and 0.7) prepared by the hydrothermal synthesis have been presented. XRD measurements displayed peaks from ZnO and $ZnCo_2O_4$ phases as well as weak lines attributed to $Co(OH)_2$ phase. The temperature and Co concentration dependence of the calculated EPR/FMR parameters (resonance fields, linewidths, integrated intensities) were studied. Three main components were recognized – a broad line attributed to nanoparticles of $ZnCo_2O_4$ phase, two narrow lines arising from Co^{2+} ions in ZnO nanoparticles, and a narrow component probably from the impurity Co_3O_4 phase.

1. INTRODUCTION

Zinc oxide (ZnO), a wide-band-gap (3.3 eV) wurzite-phase semiconductor is a very important inorganic compound, especially in a nanostructure form, due to its very broad range of applications, e.g. as gas and chemical sensors, biosensor, cosmetics, optical and electrical devices, window materials for displays, solar cells, and in drug delivery [1-3]. ZnO nanoparticles doped with transition metals are the subject of a large number of comprehensive studies and the interest is mostly due to their applications in new devices in spin-based technologies (spintronics). In many regards cobalt-doped ZnO nanomaterials may be regarded as very promising candidates of room temperature ferromagnets. In spite of extensive efforts there is still a great deal of controversy on the origin and characteristics of the observed ferromagnetism in ZnO:Co nanomaterials As the magnetic properties of these materials in different forms (nanoparticles, nanofilms, nanostructures, etc.) are concerned the situation is far from established, because there are reports that claim these materials possess intrinsic ferromagnetism, paramagnetism, extrinsic ferromagnetism, display spin glass-like behaviour or superparamagnetism [4-7]. Widely different methods and conditions of synthesis makes the goal of formation of a single general theory able to explain their magnetic properties a very difficult undertaking.

The nanocrystalline samples of ZnO/CoO can be obtained by using two methods of wet chemical synthesis: calcination and hydrothermal method.

Corresponding author: J. Typek, e-mail: Janusz.Typek@zut.edu.pl

Magnetic properties of ZnO nanocrystals doped with Co and synthesized by calcination have been studied previously [8]. A series of nanocomposites containing from 5 to 95 wt.% of CoO was obtained. Only two crystalline phases: hexagonal ZnO and cubic Co_3O_4 were identified in XRD data. The ac susceptibility measurements has shown the Curie-Weiss behaviour at high temperatures, with weak antiferromagnetic interactions. Another possible route to synthesize ZnO/CoO nanocomposites is by microwave assisted hydrothermal method [7]. The range of nominal CoO concentration for hydrothermal samples was 5 - 60 wt.%. In hydrothermal samples only two phases were found: ZnO and $ZnCo_2O_4$. For hydrothermal samples the Curie-Weiss law valid at higher temperatures gave a negative Curie-Weiss temperature indicating an effective antiferromagnetic interaction between magnetic ions. However, with increasing Co content this interaction weakened considerably and for a sample $n = 0.6$ (where n is the composition index in $(CoO)_n(ZnO)_{1-n}$ notation) ferromagnetic interaction was registered.

A key phase that is formed during hydrothermal synthesis, $ZnCo_2O_4$, is a spinel that is known to be magnetic under certain oxygenation conditions [9]. $ZnCo_2O_4$ is a transparent, p-type or n-type ferromagnetic semiconductor relevant to spintronics and wide bandgap electronics. It has a spinel structure $Zn^{2+}(Co^{3+})_2O_4$ with transition metal sites tetrahedrally and octahedrally coordinated by oxygen anions. $ZnCo_2O_4$ can be both ferromagnetic and antiferromagnetic. Antiferromagnetism is realized by Co-O-Co superexchange, ferromagnetism by Co-Co hole mediated exchange. For a large enough number of holes $ZnCo_2O_4$ can be ferromagnetic.

In the first part of this article a review of papers using the magnetic resonance techniques (electron paramagnetic resonance (EPR) and ferromagnetic resonance (FMR)) to determine the magnetic characteristics of Co-doped ZnO nanomaterials will be presented. The preparation methods used in synthesis of the discussed materials, their structural characteristics, and the main results of EPR/FMR studies of the obtained nanomaterials will be briefly described. Recently, a new series of $(CoO)_n(ZnO)_{1-n}$ nanocomposites synthesized by hydrothermal method under higher than previously applied pressure was synthesized. It enabled to obtain more concentrated Co nanocomposites (up to $n = 0.7$). EPR/FMR study of these samples will be described in the second part of this paper. Magnetic resonance spectra registered in 4 - 290K temperature range will be analysed and information about magnetic systems responsible for the observed spectra and involved magnetic interactions will be deduced.

2. REVIEW OF PAPERS REPORTING MAGNETIC RESONANCE STUDY OF Co-DOPED ZnO

In Table 1 the relevant information is presented on the published papers dealing with the magnetic resonance studies of Co-doped ZnO nanomaterials [10-37]. Three important features of the presented paper were selected and briefly described: preparation method of the studied nanomaterials, the morphology of obtained samples (column 2), and main conclusions drawn from EPR/FMR studies (column 3).

The methods of samples syntheses were very diverse, resulting in different final forms of the studied nanosamples. The following sample forms were produced: thin and thick films [10,12-14,20,26,28], nano- and microcrystals [19,22,25.27], nanopowders [11,15,17,30-34,37], nanorods [21,23,25], nano- and microwires [16,36], and quantum dots [29]. To synthesize thin films and layers on different substrates, the epitaxy, pulsed lase deposition, plasma assisted MBE, and atomic layer deposition methods were used. Nanopowders were produced mostly by sol-gel method, using co-precipitation and wet chemical synthesis. Nanorods and nanowires were synthesized by high-pressure pulsed laser deposition, optical furnace, and by non-aqueous sol-gel methods.

Concentration of Co ions in samples in Table 1 varies in a rather broad range (from close to zero up to 30%). As the solubility limit of Co in ZnO matrix is concerned there are various values reported, depending mostly on sample preparation method [38-42]. For many transition metal ions in the diluted magnetic oxides this limit is usually low. For Co-doped bulk ZnO it is close to 10 at.% [38]. Samples prepared by pulsed laser deposition or ion implantation show the highest solubility limit. For films prepared by pulsed laser deposition technique a very high value of 40 at.% was reported [39]. On the other hand, a strong phase separation and formation of Co_3O_4 was observed for films prepared by meta-organic deposition with 5 at.% of cobalt [40]. The solubility limit of 15 at.% was observed in nanoalloys [41], while for samples prepared by sol-gel and RF sputtering it is close to 12 at.% [42].

Before discussing EPR/FMR results of Co-doped ZnO nanomaterials it will be instructive to recall similar results obtained on bulk ZnO undoped and

Table 1. Overview of papers reporting magnetic resonance studies of Co-doped ZnO nanomaterials.

Ref.	• Preparation method • Morphology of obtained samples	Main conclusions from EPR/FMR study
10	• Epitaxy. • Epitaxial (Zn,Co)O layers with 10% Co concentration	200 G broad anisotropic single line with *g* factors close to those of the isolated Co^{2+} ion. EPR signal follows a Curie-Weiss law with a critical temperature of +12K. No evidence of ferromagnetism at RT.
11	• Two methods: RT wet synthesis and microwave synthesis. • Only ZnO phase is obtained, without any XRD trace of dopant or its oxides. Average particle size of ZnO phase was in 20 - 70 nm range	Broad line at $g \sim 4.3$ ($T = 10$K) due to Co^{2+} ions, no hyperfine structure lines because of high (5%) Co loading. The interaction between Co^{2+} ions may be the origin of ferromagnetism in samples hydrogenated at 573K.
12	• Pulsed laser deposition in an atmosphere of O_2 and He on silica substrate. • Nanostructured $Zn_{1-x}Co_xO$ films (~ 1 μm thickness, x = 0 - 0.10) crystallized in the wurtzite structure.	Co^{2+} ions substitute in Zn sites in $Zn_{1-x}Co_xO$ nanoclustres. A single EPR line is attributed to the $\|-1/2\rangle \rightarrow \|1/2\rangle$ transition in the lower Kramer's doublet.
13	• Plasma-assisted MBE. • 1 μm epitaxial thin films of $Zn_{1-x}Co_xO$ (x varied from 0.003 to 0.005) on sapphire substrate.	Co^{2+} ($S = 3/2$) substitutes Zn^{2+} in ZnO lattice and has a huge single ion anisotropy, $D = 2.76$ cm^{-1}. FM of ZnO:Co would be an "easy plane" ferromagnet.
14	• Plasma-assisted MBE. • Single crystalline $Zn_{1-x}Co_xO$ (x = 0.001–0.075) thin films.	Co^{2+} exchange pairs were observed. A combined effect of exchange and dipolar broadening can explain the linewidth variation with Co content and temperature.
15	• Wet colloid chemical method. • Nanoparticles with sizes in the 3 - 8 nm range. Co doping concentration in the range 1 - 10%.	A broad powder-like spectrum indicate Co ions are substitutionally incorporated on Zn sites. Paramagnetic behaviour of EPR spectra excludes ferromagnetism.
16	• High-pressure pulsed laser deposition on sapphire substrate. • Nanowires of a length of about 1 μm aligned perpendicular to the substrate surface. They have hexagonal cross section and their diameters in 60 nm up to 150 nm range. The lowest nominal concentrations of Co was 5 at.%.	Anisotropic EPR spectra of isolated Co^{2+} on Zn sites were detected. Two different paramagnetic components were deduced from temperature dependence of the EPR spectra.
17	• Sol–gel-synthesis, powders processed at 350 °C. • Nanoscale $Zn_{1-x}Co_xO$ powders with $0 \le x \le 0.12$.	Substitutional doping of Co at the tetrahedral Zn^{2+} sites for $x < 0.03$, additional interstitial incorporation of Co for bigger x. Paramagnetic behaviour in $Zn_{1-x}Co_xO$ with increasing antiferromagnetic interactions as x increased to 0.10, and a weak ferromagnetic behaviour for the sample with x = 0.12.
18	• Thermal decomposition of zinc acetate and a dopant precursor in trioctylamine. • 2.1 and 1.1% Co doped ZnO nanowires.	Two EPR signals at helium temperatures with *g*-factors 4.43 and 2.23.
19	• Wet chemical method with chemical surface modifications.	Three different EPR signals were registered: one coming from substitutional Co^{2+} in the core of

	• Three kinds of samples: agglomerated nanocrystals with an average size of 6 nm, polystyrene/ZnO:Co nanocomposite, and ZnO:Co nanocrystals capped with ZnSe.	nanoparticles (same parameters as in bulk) and the other two caused by locally distorted environment in the shells.
20	• Pulsed laser deposition. • Thin films of highly Co-doped $Zn_{0.7}Co_{0.3}O$.	Two Co species were detected: one Co^{2+} incorporated in ZnO in Zn site and the other in randomly oriented metallic Co nanoparticles. From the later an FMR spectrum was measured and the effective magnetisation $4\pi M$ = 800 G at 300K was calculated.
21	• Non-aqueous sol–gel route based on benzyl alcohol as solvent • 3 and 5 mol.% Co-doped ZnO nanorods (with an average diameter ~40 nm).	A very broad signal with an irregular lineshape, probably the ferromagnetic resonance.
22	• Two methods: wet chemical method with chemical surface modifications and high-pressure pulsed laser deposition on sapphire substrate. • Two types of samples: nanocrystals, polystyrene/ZnO:Co nanocomposites, ZnO:Co nanocrystals capped with ZnSe, and nanowires with hexagonal cross section and diameters in 60 nm up to 150 nm range, about 1 μm in length, aligned perpendicular to the substrate surface.	For Co doped ZnO nanowires two EPR signals were detected arising from substitutional Co^{2+} ions in slightly different environments. For nanocrystal samples three distinct EPR signals were detected due to the core and different locally distorted shells. No evidence of FM was found.
23	• Non-aqueous sol-gel method based on benzyl alcohol as a solvent. • 3% and 5% ZnO:Co nanorods.	A very broad, with irregular lineshape, probably FMR signal due to the coupling of Co cations through zinc interstitial.
24	• Wet chemical method. • Almost spherical $Zn_{1-x}Co_xO$ (x = 0.01 and 0.03) microcrystals (170 and 340 nm in sizes).	EPR spectra typical for isolated Co^{2+} in powders. At high temperatures the Curie-Weiss behaviour of integrated intensity indicates FM interaction between Co^{2+} ions.
25	• Wet chemical method. • $Zn_{1-x}Co_xO$ (x = 0.01 and 0.03) microcrystals.	Typical EPR lines for isolated Co^{2+} ions in powder sample. Temperature dependence of the EPR integrated intensity reveals FM interaction between Co^{2+} ions.
26	• Atomic layer deposition. • Uniform and non-uniform polycrystalline thin films with columnar growth on different substrates (sapphire, glass, silicon).	Uniform layers produced only paramagnetic response. Metallic Co clusters are responsible for ferromagnetism.
27	• Autocombustion method. • $Zn_{0.8}Co_{0.2}O$ agglomerated nanoparticles with an average nanocrystals size of 21 nm.	A broad FMR line is observed at RT. No metallic Co signal in magnetic resonance spectra.
28	• Pulsed laser deposition. • 500 nm thick layer of ZnO:Co (4%).	EPR spectrum consists of a single Lorentzian line, its linewidth, g-factor and integrated intensity display a change at 220K. Curie-Weiss type dependence of integrated intensity indicates FM interaction between Co^{2+} ions.
29	• Wet chemical method. • Quantum dots of $ZnO/Zn(OH)_2$ with core-shell structure. Nanocrystals diameters were in 2 - 5 nm range.	EPR spectra of substitutional Co^{2+} ion in ZnO described by the standard axial spin-Hamiltonian for electron spin S = 3/2 with anisotropic g-factor and anisotropic hyperfine interaction constant. The shape of the EPR spectrum of cobalt ions changed

		as a result of Co^{2+} coupling with optically created shallow donors, demonstrating interaction between the magnetic ion and donor electron in confined system of ZnO quantum dots.
30	• Forced hydrolysis method. • $Zn_{1-x}Co_xO$ nanoparticles (~9 nm) with x ranging from 0 to 0.2.	The doped samples showed spectra corresponding to Co^{2+}. The variation of the integrated EPR signal intensity with x showed a maximum at x = 0.025. The observed changes in the magnetic properties are related to changes in the electronic structure of ZnO nanoparticles caused by dopant incorporation.
31	• Sol-gel method (citrate route) • Nanoparticles $Zn_{1"x}Co_xO$ ($0.01<x<0.05$) with sizes in 20 - 27 nm range	Two main EPR lines (at g ~ 4.41 and 2.20) from Co^{2+} in axial symmetry. Additional lines (g ~ 2.0) for samples with $x > 0.04$ from free shallow radicals. Co^{2+} ions are ferrimagnetically coupled.
32	• Co-precipitation method. • Nanoparticles with an average crystallite sizes in 18 - 27 nm range and Co concentrations in 3 -18 at.% range.	Gaussian single broad FMR line (g-factor depending on Co concentration) which arises from long range exchange interaction and from transitions within the ground state of the ferromagnetic domain. No presence of Co-metal clusters and Co-oxide precipitates.
33	• Wet-chemical synthesis route using the SimAdd technique. • $Zn_{1-x}Co_xO$ nanoparticles (x = 0.05, 0.10, 0.15) with spherical and polyhedral shapes and tendency to agglomeration. Particles sizes in 28 - 37 nm range. In x = 0.15 sample the presence of Co_3O_4 was detected.	Integrated intensity of EPR lines decreases with Co concentration increase up to 10% Co. For higher Co concentration EPR signal from Co_3O_4 was registered. Ferromagnetic interaction between substitutional Co^{2+} ions was detected in the high temperature range in the temperature dependence of integrated intensity.
34	• Co-precipitation method. • $Zn_{1-x}Co_xO$ nanoparticles (x = 0.05, 0.10, 0.15) with sizes in 29 -35 nm range.	An intense single and broad line at g = 2.24 at RT that shifts slightly towards higher magnetic fields with increasing cobalt doping concentration.
35	• Two chemical hydrolysis methods, using diethylene glycol (rod-like samples) and denatured ethanol (spherical samples). • Rod-like and spherical samples of $Zn_{1-x}Co_xO$ nanoparticles (x = 0.005, 0.025, 0.050, 0.100)	The presence of both paramagnetic Co^{2+} ions exhibiting sharp lines, and FM coupled ions, exhibiting very broad FMR lines. An EPR signal due to surface oxygen vacancies was observed in rod-like samples. Oxygen vacancies were involved in ferromagnetic coupling.
36	• Optical furnace method. • Cobalt-doped ZnO micro-wires with Coconcentration in the range 0 – 5%.	Isolated Co^{2+} ions in Zn^{2+} sites with spin Hamiltonian parameters like in bulk ZnO and distant pairs of Co^{2+} ions deduced from satellite lines.
37	• Sol-gel method (citrate route) • Nanoparticles $Zn_{1-x}Co_xO$ (x = 0.01, 0.03, 0.05, 0.08, 0.10) strongly agglomerated of different sizes less than 100 nm.	For samples with x = 0.01 and 0.03 high spin Co^{2+} substitutes for Zn^{2+}, for x = 0.05 part of cobalt ions is in low spin Co^{3+} (S = 0) state, for $x > 0.05$ an impurity phase is formed.

doped with Co. There is a large number of papers devoted to EPR study of bulk ZnO undoped (but with impurities and defects) and doped with Co ions that started with the paper of Estle and De Wit [43]. A review of all EPR papers dealing with impurities, intrinsic defects, and doping elements in bulk ZnO is given by Steher et al. [44]. An important role of oxygen defects in bulk ZnO and their EPR study is reviewed by Vlasenko [45]. An interesting aspect of strong non-uniformity of Co distribution in ZnO bulk single crystal leading to many Co-Co pairs, even when dopant concentration is low, is discussed by Azamat et al. [46]. It is well established that the ground state of Co^{2+} at a tetrahedral site in the ZnO host lattice is described by S=3/2 spin Hamiltonian containing the Zeeman and zero-field splitting terms. As the latter term is bigger than the former (the zero-field splitting constant D = 2.76 cm^{-1}) there will be

splitting of the ground state on two doublets. In consequence, a low frequency EPR study ($\nu \approx 10$ GHz) will only observe transitions in the low lying doublet $S_z = \pm 1/2$ and thus a single line with $g_{||} = 2.24$, $g_{\perp} = 4.55$ [13,14].

The most important question the authors try to answer is whether a specific sample displays ferromagnetism at RT and if so what is the mechanism that produces that state at so high temperature. Of course that later question could not be answered taking into consideration only magnetic resonance study. Usually, dc/ac magnetisation measurements have to be taken into account to obtain a comprehensive picture of magnetic interactions. Most of samples in Table 1 displayed only paramagnetic signals from Co^{2+} ions that entered substitutionally into the Zn^{2+} sites. Temperature dependence of the integrated intensity of these EPR signal usually displayed the Curie-Weiss behaviour with positive Curie-Weiss constant indicating ferromagnetic interaction between Co^{2+} ions. For higher concentrations of cobalt ions, the EPR spectra arising from interstitial incorporation of Co^{2+}, from metallic cobalt clusters, and Co_3O_4 phase, were recorded. Only in a few cases a broad FMR signal was recorded, sometimes accompanied by a paramagnetic EPR line [11,20,21,23,26,27, 32,35]. The origin of the FMR line was attributed to metallic cobalt nanoclusters, direct magnetic interaction between cobalt ions or ferromagnetic interaction involving oxygen vacancies. Taking into account a broad spectrum of preparation methods and conditions of synthesis it is not surprising that such very different magnetic behaviours are observed. Due to the fact that so many factors influence the magnetic state of ZnO:Co nanomaterials, it would be difficult to present a coherent picture of magnetism in these samples. The most important factors seems to be: the growth and the annealing temperatures, the annealing atmosphere, the presence of oxygen vacancies, the content and the distribution of Co ions, the presence of secondary phases, and the sizes of nanoparticles. They all should be taken into account when discussing the problem of intrinsic (i.e. mediated by carriers or intentional defects inside the host material) or extrinsic (i.e. dopant-introduced defects, secondary phases, metallic clusters) origin of ferromagnetism in these nanomaterials.

3. EXPERIMENTAL

Nanocomposites of the general formula $(CoO)_n(ZnO)_{1-n}$ (where the composition index $n = 0.4$, 0.5, 0.6, and 0.7) were prepared by using a microwave hydrothermal synthesis at pressure 3.9 MPa applied for the reaction time of 15 min. At first, a mixture of cobalt and zinc hydroxides was obtained by addition of 2 M solution of KOH to the 20% solution of a proper amount of $Zn(NO_3)\cdot 6H_2O$ and $Co(NO_3)\cdot 6H_2O$ in water and then treated in a solvothermal microwave reactor. Next, the obtained materials were washed with deionized water to remove salt residues. Finally, the materials were dried at 100 °C for 24 h.

The morphology of samples was investigated by using the scanning electron microscope (SEM, Hitachi) followed by the phase composition of samples determined by the X-ray diffraction (XRD, $Co_{K\alpha}$ radiation, X'Pert Philips). The specific surface area of the nanopowders was determined using the Brunauer–Emmett–Teller (BET) method with the equipment Gemini 2360 of Micromeritics. The helium pycnometer AccuPyc 1330 of Micromeritics was applied to determine the density of powders. Magnetic resonance study was carried out on a conventional magnetic resonance spectrometer Bruker E 500 with 100 kHz magnetic field modulation equipped with an Oxford helium-flow cryostat.

4. RESULTS AND DISCUSSON

According to the results of XRD analysis, the XRD spectra revealed the presence of ZnO, cobalt hydroxide $Co(OH)_2$, and $ZnCo_2O_4$ phases (Fig. 1). Spinel phase $ZnCo_2O_4$ content increases with the increase of CoO content in samples, while the ZnO content decreases simultaneously. The mean crystallite sizes of the detected phases were determined using Scherrer's formula. In particular,

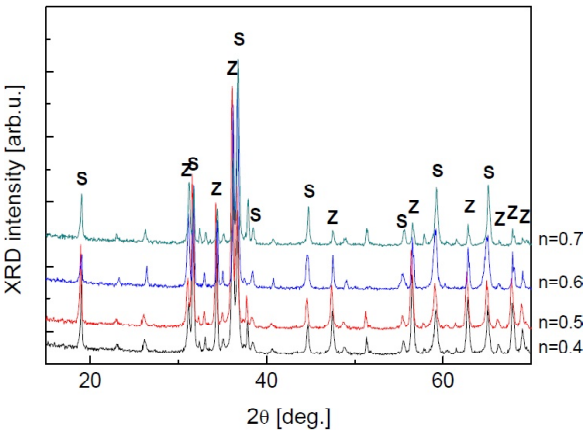

Fig. 1. XRD patterns for nCoO/(1-n)ZnO nanocomposites with n = 0.4, 0.5, 0.6, and 0.7. Peaks attributed to ZnO are marked as *Z*, peaks marked as *S* to $ZnCo_2O_4$. The not marked peaks are attributed to $Co(OH)_2$.

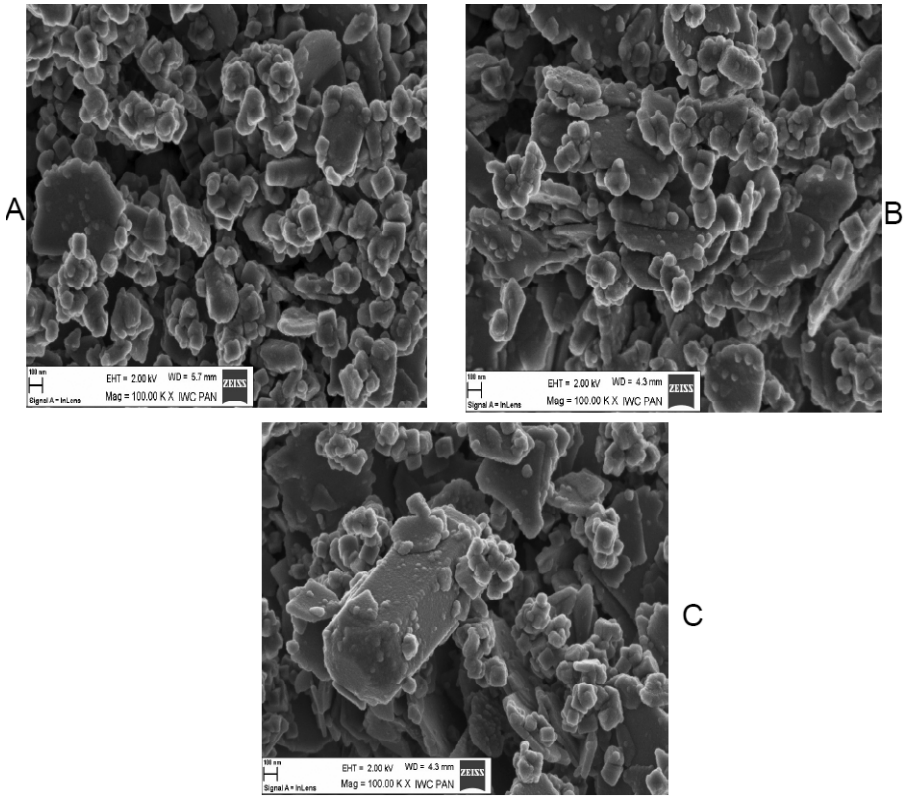

Fig. 2. SEM images of nCoO/(1-n)ZnO nanocomposites with different composition index: (a) n = 0.5; (b) n = 0.6; (c) n = 0.7.

the mean crystallite sizes of $ZnFe_2O_4$ varied from 8 to 12 nm. SEM images of nCoO/(1-n)ZnO nanocomposites with different composition indexes n = 0.5, 0.6, and 0.7 are shown in Fig. 2. SEM study allowed to distinguish three different types of morphology: small spheroidal forms, large plates, and rods (Fig. 2). The values of the helium density of investigated samples were in 4.6 - 4.7 g/cm^3 range, the specific surface area in 19 - 21 m^2/g range. The obtained results showed that the helium density and specific surface area is at a similar level in all samples. Low density may be due to the presence of cobalt hydroxide $Co(OH)_2$, the presence of this phase was confirmed by XRD analysis.

A selection of the registered magnetic resonance spectra of four investigated samples, taken at different temperatures, is illustrated in Figs. 3a-3d. Three main spectral features are easily to notice: a very broad line visible in n = 0.4, 0.5, and 0.7 samples, and three relatively narrow, asymmetrical lines (designated as N1, N2, and N3) visible at low temperatures in all samples. To examine the temperature and composition changes of these magnetic resonance components, the obtained spectra were fitted with Lorentzian lineshape lines. An example of such fitting, in case of n = 0.5 sample, registered at T = 50K, is presented in Fig. 4. For the broad line one Lorentzian line (but with its counterpart in negative magnetic fields, as required for very broad lines) was sufficient to properly account for this symmetrical spectral component. Although this simple fitting method is very crude, it might provide necessary parameters (A - amplitude, H_r - resonance field, and ΔH_{pp} – peak-to-peak linewidth) with accuracy that is satisfactory for introductory, general analysis of the registered magnetic resonance spectra. The knowledge of these parameters allows to calculate another important quantity – the integrated intensity, $I_{int} = A \cdot (\Delta H_{pp})^2$, which is proportional to the magnetic susceptibility of the spin system on microwave frequency.

The broad line is visible in the whole investigated temperature range, but its amplitude is large only in 20 – 90K interval. An exception is sample n = 0.6, in which this line is so broad as to make it unnoticeable (Fig. 3c). The resonance field H_r of the broad line is in 2.5 – 3.5 kG range in 25 -50K interval. It can be notice that the higher the Co content, the bigger the resonance field. Outside 25 – 50K temperature range H_r diminishes rapidly and is close to zero (Fig. 5, upper panel). This result can be interpreted as the appearance of an internal magnetic field that compensates externally applied magnetic field. The linewidth of the broad line varies with

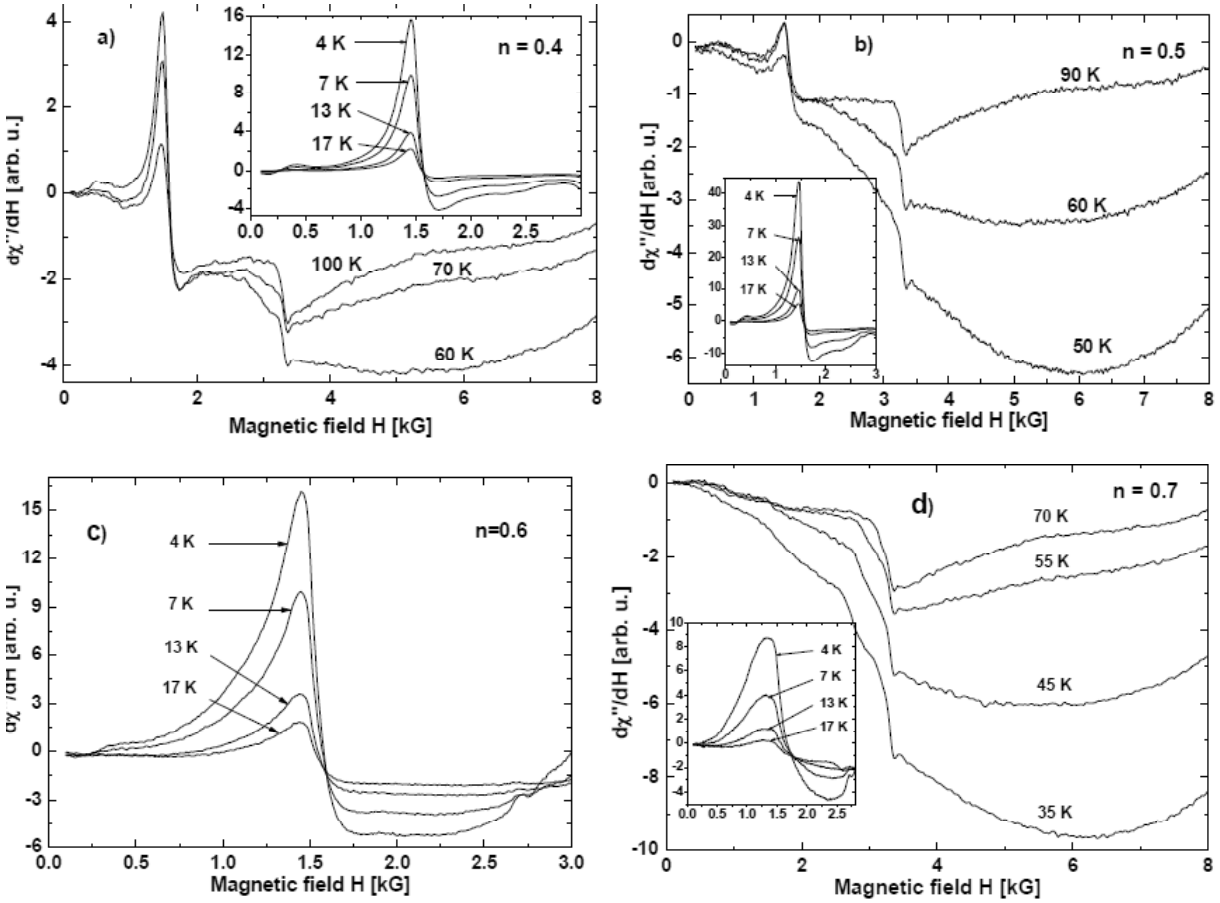

Fig. 3. Magnetic resonance spectra of the *n*CoO/(1-*n*)ZnO nanocomposites: (a) *n* = 0.4; (b) *n* = 0.5; (c) *n* = 0.6; (d) *n* = 0.7. The insets in (a), (b), and (d) show spectra of the low-field narrow line (designated as N1) registered in the low temperatures range.

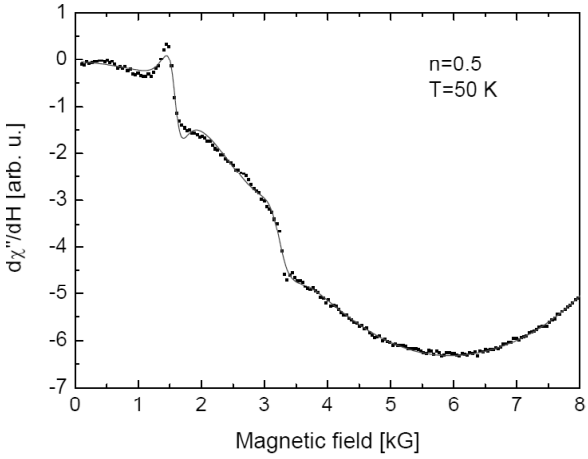

Fig. 4. Magnetic resonance spectrum of *n* = 0.5 sample at *T* = 50K (points) and the fitted spectrum of the broad line (solid line).

temperature and also with Co content (Fig. 5, middle panel). Generally, it increases with decreasing temperature, but seems to have two local maxima, one in 60 - 90K range (smaller) and the other in 5 - 15K range (bigger). This fact points out on the existence of more than one magnetic entity participating in the formation of the broad line. Analysis of the temperature dependence of the integrated intensity (Fig. 5, bottom panel) might serve as another evidence to confirm this suggestion. The integrated intensity of the broad line increases with temperature decrease, but has a local maximum at 65K and another additional one at 15K, but only for *n* = 0.6 and 0.7 samples. These double maxima dependence can be possibly explained if more than one magnetic component is involved in formation of the broad line, especially in samples with high cobalt content.

Taking into account the results of our magnetic resonance measurements it could be argued that the broad line is a ferromagnetic resonance due to (mostly) $ZnCo_2O_4$ agglomerated nanoparticles. Because of agglomeration no superparamagnetic resonance (narrow line close to $g \approx 2$) is observed. For higher concentration of CoO in an initial material (for samples *n* = 0.6 and 0.7) other ferromagnetic components participating in formation of the broad line are possible (e.g. cobalt oxides or metallic cobalt nanoparticles) what is suggested by two maxima in

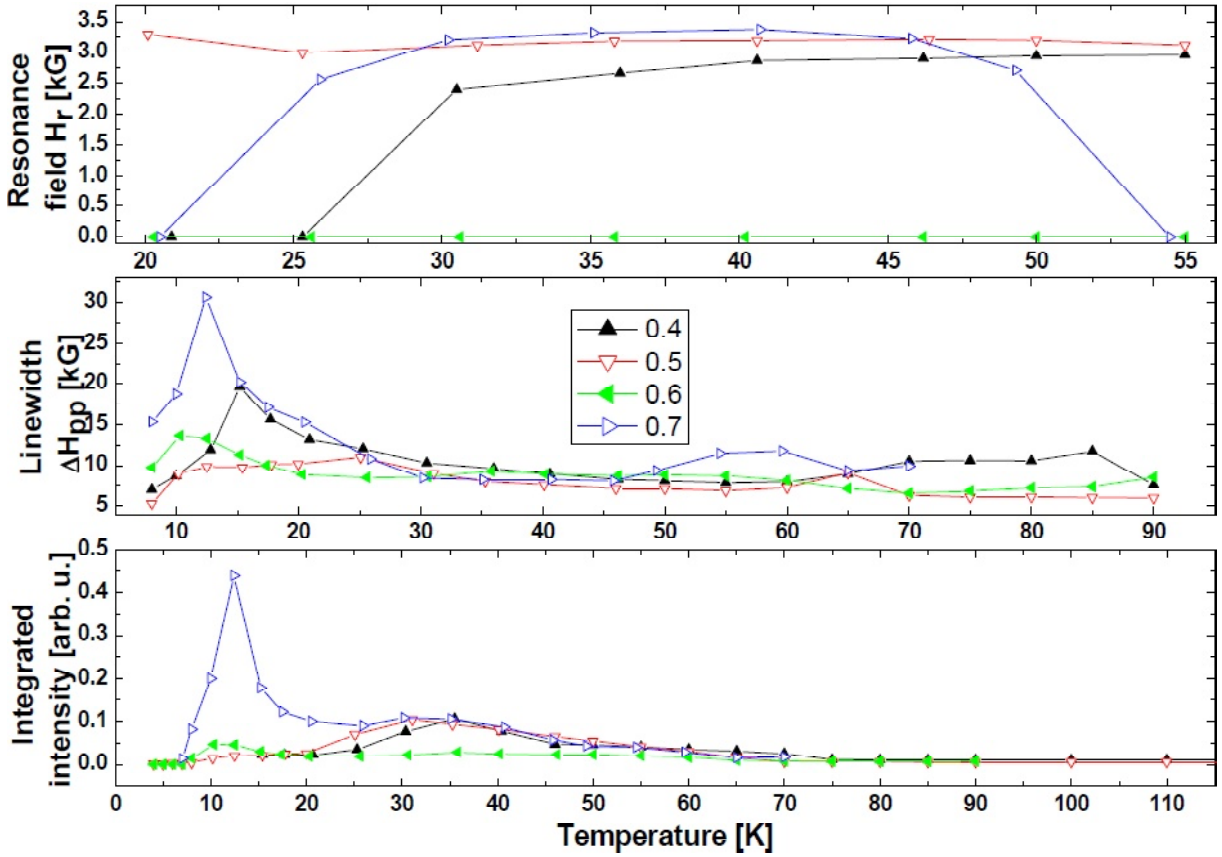

Fig. 5. Temperature dependence of the resonance field (top panel), peak-to-peak linewidth (middle panel), and integrated intensity (bottom panel) of the broad line in four investigated samples.

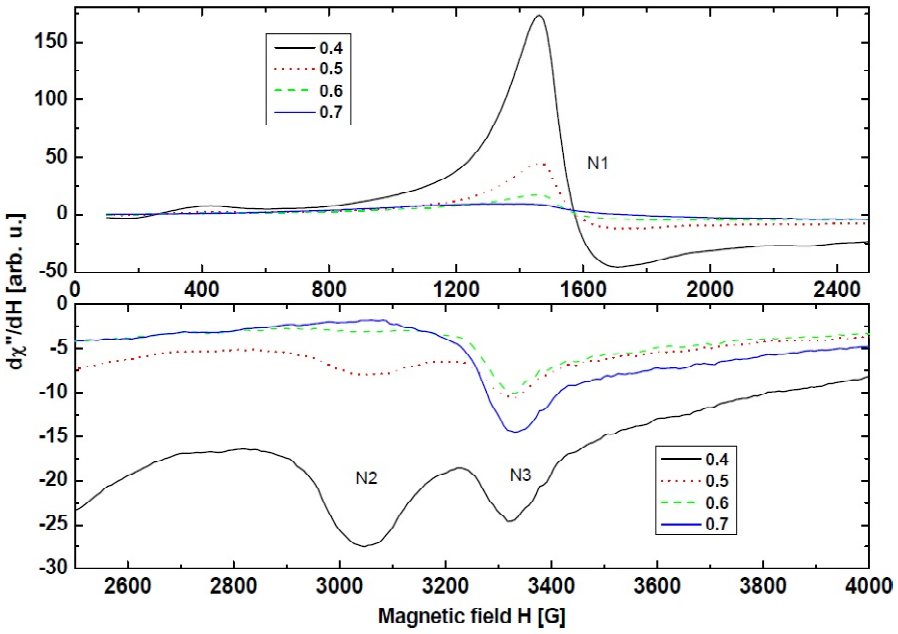

Fig. 6. Magnetic resonance spectra of three narrow lines (N1 – top panel, N2 and N3 – bottom panel) in four investigated samples registered at T = 4K.

the temperature dependence of integrated intensity and in linewidth. These extra phases were not registered by XRD, but this technique is not so sensitive to impurity detection as EPR.

There are three relatively narrow lines N1, N2, and N3 visible in the registered spectra. Fig. 6 shows these lines in four investigated samples at T = 4K. Two narrow lines, one in low magnetic field (line N1, g ~ 4.31) and the other near 3 kG (line N2, g ~ 2.28)

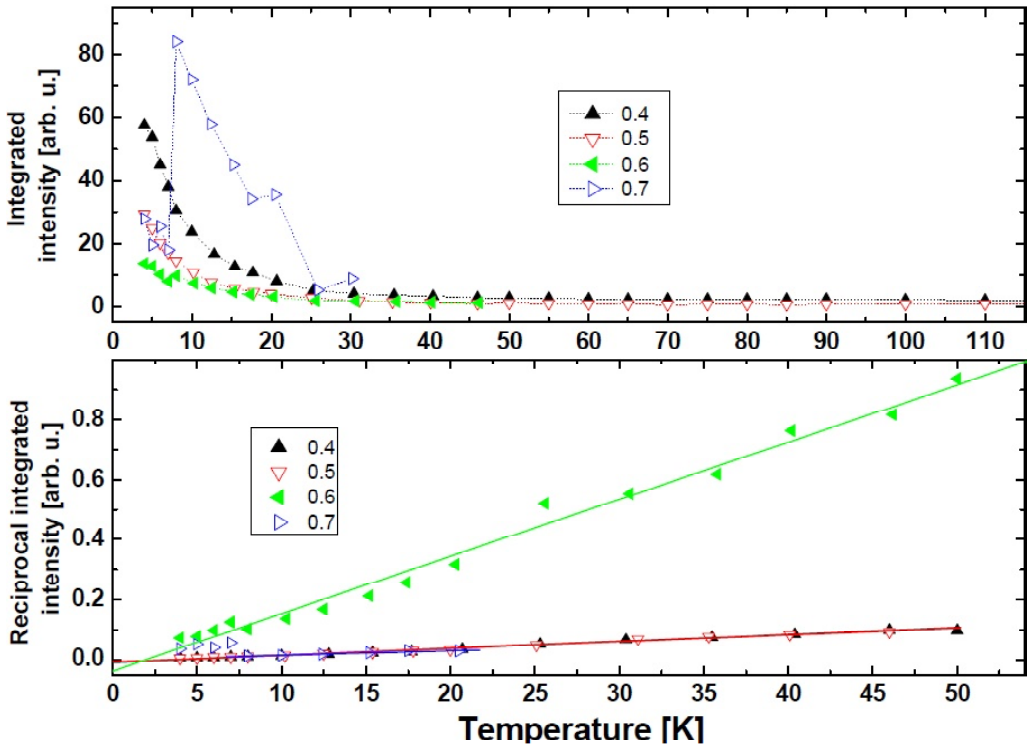

Fig. 7. Temperature dependence of the integrated intensity (top panel), and the reciprocal integrated intensity (bottom panel) of the sum of N1 and N2 lines in four investigated samples.

can be only registered in the low temperature range (T < 120K). They show very similar behaviour as a function of Co concentration – the higher the concentration of Co (smaller n index), the smaller the EPR amplitude of these lines. It follows that they belong to the same magnetic component and they are located in ZnO phase, whose concentration diminishes with an increase of the composition index n. As a matter of fact they belong to the same powder-like EPR spectrum and the more intense N1 line can be identified as the perpendicular component ($g_{\perp}$), while N2 line as the parallel component ($g_{||}$). Our measured g-factors are not very different from the values found for Co^{2+} in tetrahedral sites in bulk ZnO. The integrated intensity of this component (being the sum of two lines) increases with temperature decrease and at low temperatures (T < 50K) the Curie-Weiss law, $I_{int}(T) = C/(T-T_0)$, is fulfilled (Fig. 7). In this equation C is a constant related to magnetic moment of the spin centre and T_0 is the Curie-Weiss temperature. The sign of T_0 provides information about the type of an effective interaction, ferromagnetic if T_0 is positive, antiferromagnetic if T_0 is negative. In the case of N1 and N2 lines T_0 was positive for all samples. The calculated values of T_0 for samples with n = 0.4, 0.5, 0.6, and 0.7 are 3.9, 3.4, 2.0, and 0.3K, respectively. Thus in our samples there is a rather weak ferromagnetic interaction between isolated Co^{2+} ions and its strength diminishes with the increase of cobalt concentration.

The third unsymmetrical narrow line (N3, g ~2.06) shows in comparison to N1 and N2 lines quite different behaviour as a function of temperature (see Fig. 3) and cobalt concentration (Fig. 6). It is visible already at RT and its amplitude seems to not depend on the concentration index n. This suggests that it may be due to some paramagnetic secondary phase not registered in XRD study. Cobalt oxide is a possible candidate for such a phase. Bulk cobalt oxide (Co_3O_4) has a normal cubic spinel structure with eight Co^{2+} occupying tetrahedral A-sites (magnetic moment 4.14 μ_B) and sixteen Co^{3+} ions on octahedral A-sites (diamagnetic) [47]. Antiferromagnetic coupling of A-sites ions brings about the antiferromagnetic ordered phase below Neel temperature (reported in 30 – 40K range). It has been observed that in case of antiferromagnetic nanoparticles the Neel temperature is reduced and many new magnetic phenomena might appear (weak ferromagnetism, spin canting, exchange bias effect) due to uncompensated surface or core spins. EPR study of Co_3O_4 nanoparticles has showed an unsymmetrical line at $g \approx 2$ with linewidth comparable to our N3 component [48]. Thus it is quite possible that N3 spectrum arises from Co_3O_4 nanoparticles present in all our samples in small concentration.

As the XRD study of our samples has found traces of $Co(OH)_2$ phase, the question arises about visibility of this phase in registered EPR spectra. EPR study of cobalt hydroxide $Co(OH)_2$ was reported by Al-Ghoul *et al.* [49]. This compound exhibits two polymorphs with hexagonal layered structures denoted as α- and β-$Co(OH)_2$. The former polymorph shows thermodynamic instability and transforms to the stable β-form. Cobalt ions (only in Co^{2+} form) occupy both tetrahedral and octahedral sites in a-$Co(OH)_2$, while only octahedral sites in β-phase. At RT both phases are EPR silent, but below 200K a signal was appeared in α-$Co(OH)_2$ (a single line with g_{eff} ~ 2.21, linewidth 40 mT), gaining in intensity on further cooling. No EPR signal was registered for β-$Co(OH)_2$ in the whole temperature range, what is not unusual taking into account the octahedral surrounding of Co^{2+} ions [49]. Therefore it could be concluded that in our samples cobalt hydroxide appears in the stable β-form and is EPR silent.

5. CONCLUSIONS

Review of papers describing magnetic resonance studies of Co-doped ZnO nanomaterials has shown a broad spectrum of investigated types of nanosamples (nanoparticles, thin layers, nano-rods and –wires, quantum dots) produced by very different methods. Most samples showed paramagnetic spectrum of Co^{2+} ions in Zn^{2+} sites if cobalt concentration was low (below 5%), but additional spectral components (from metallic clusters or secondary phases) were observed on higher doping. Magnetic resonance study of a new series of *n*CoO/(1-*n*)ZnO nanocomposites with composition index *n* = 0.4, 0.5, 0.6, and 0.7 synthesized by hydrothermal method has revealed three main features in the registered spectra – a broad line due mostly to $ZnCo_2O_4$ agglomerated nanoparticles, two narrow lines attributed to isolated, but interacting Co^{2+} ions in ZnO phase, and one narrow, unsymmetrical line, probably from Co_3O_4 nanoparticles. Despite heavy Co doping in our samples the isolated Co^{2+} ions in ZnO phase are present as in a lightly doped ZnO bulk crystals. The dominating phase in highly Co-doped ZnO nanoparticles is $ZnCo_2O_4$, but as the nanoparticles are strongly agglomerated no superparamagnetic phase is observed at high temperatures.

REFERENCES

[1] Z.L. Wang // *J. Phys.: Condens. Mat.* **16** (2004) R829.

[2] A. Janotti and Ch.G. Van de Walle // *Rep. Prog. Phys.* **72** (2009) 126501.

[3] A. Kolodziejczak-Radzimska and T. Jesionowski // *Materials* **7** (2014) 2833.

[4] G. Lawes, A.S. Risbud, A.P. Ramirez and Ram Seshadri // *Phys. Rev. B* **71** (2005) 045201.

[5] K. Ueda, H. Tabota and T. Kamai // *Appl. Phys. Lett.* **79** (2001) 988.

[6] O. Toulemonde and M. Gaudon // *J. Phys. D: Appl. Phys*. **43** (2010) 045001.

[7] I. Kuryliszyn-Kudelska, B. Hadžić, D. Sibera, M. Romčević, N. Romčević, U. Narkiewicz, W. Łojkowski, M. Arciszewska and W. Dobrowolski // *J. Alloy. Compd*. **561** (2013) 247.

[8] I. Kuryliszyn-Kudelska, W. D. Dobrowolski, L. Kilanski, B. Hadžić, M. Romcevic, D. Sibera, U. Narkiewicz and P. Dziawa // *J. Phys.: Confer. Ser.* **200** (2010) 072058.

[9] H.J. Kim, I.C. Song, J.H. Sim, H. Kim, D. Kim, Y.E. Ihm and W.K.C. Choo // *J. Appl. Phys.* **95** (2004) 7387.

[10] N. Jedrecy, H.J. von Bardeleben, Y. Zheng and J-L. Cantin // *Phys. Rev B* **69** (2004) 041308(R).

[11] G. Glaspell, P. Dutta and A. Manivannan // *J. Clust. Sci.* **16** (2005) 523-536.

[12] I. Ozerov, F. Chabre and W. Marine // *Mater. Sci. Eng. C*, **25** (2005) 614-617.

[13] P. Sati, R. Hayn, R. Kuzian, S. Régnier, S. Schäfer, A. Stepanov, C. Morhain, C. Deparis, M. Laügt, M. Goiran and Z. Golacki // *Phys. Rev. Lett.* **96** (2006) 017203.

[14] P. Sati, V. Pashchenko and A. Stepanov // *Fiz. Nizk. Temp.* **33** (2007) 1222.

[15] N. Volbers, H. Zhou, C. Knies, D. Pfisterer, J. Sann, D.M. Hofmann and B.K. Meyer // *Appl. Phys. A* **88** (2007) 153.

[16] A.O. Ankiewicz, M.C. Carmo, N.A. Sobolev, W. Gehlhoff, E.M. Kaidashev, A. Rahm, M. Lorenz and M. Grundmann // *J. Appl. Phys.* **101** (2007) 024324

[17] J. Hays, K. M. Reddy, N. Y. Graces, M. H. Engelhard, V. Shutthanandan, M. Luo, C. Xu, N. C. Giles, C. Wang, S. Thevuthasan and A. Punnoose // *J. Phys.: Condens. Mat.* **19** (2007) 266203.

[18] G. Clavel, N. Pinna and D. Zitoun // *Phys. Stat. Sol. A* **204** (2007) 118.

[19] A.S. Pereira, A.O. Ankiewicz, W. Gehlhoff, A. Hoffmann, S. Pereira, T. Trindade,

M. Grundmann, M.C. Carmo and N.A. Sobolev // *J. Appl. Phys*. **103** (2008) 07D140.
[20] H. J. von Bardeleben, N. Jedrecy and J. L. Cantin // *Appl. Phys. Lett.* **93** (2008) 142505
[21] I. Djerdj, G. Garnweitner, D. Arcon, M. Pregelj, Z. Jaglicic and M. Niederberger // *J. Mater. Chem.* **18** (2008) 5208-5217.
[22] A.O. Ankiewicz, W. Gehlhoff, J.S. Martinis, A.S. Pereira, |S. Pereira, A. Hoffmann, E.M. Kaidashev, A. Rahm, M. Lorenz, M. Grundmann, M.C. Carmo, T. Trindade and N.A. Sobolev // *Phys. Stat. Sol. B* **246** (2009) 766.
[23] I. Djerdi, Z. Jaglicic, D. Arcon and M. Niederberger // *Nanoscale* **2** (2010) 1096.
[24] A. Popa, D. Toloman, O. Raita, A.R. Biris, G. Borodi, T. Mustafa, F. Watanabe, A.S. Biris, A. Darabont and L.M. Giurgiu // *Cent. Eur. J. Phys.* **9** (2011) 1446.
[25] O. Raita, A. Popa, D. Toloman, M. Stan, A. Darabont and L. Giurgiu // *Appl. Mag. Res*. **40** (2011) 245.
[26] M.I. Lukasiewicz, A. Wojcik-Glodowska, E. Guziewicz, A. Wolska, M.T. Klepka, P. Dluzewski, R. Jakiela, E. Lusakowska, K. Kopalko, W. Paszkiewicz, L. Wachnicki, B.S. Witkowski, W. Lisowski, M. Krawczyk, J.W. Sobczak, A. Jablonski and M. Godlewski // *Semicond. Sci. Tech.* **27** (2012) 074009.
[27] Y. Koseoglu // *J. Supercond. Nov. Magn.* **26** (2013) 485.
[28] B. Cieniek, I. Stefaniuk and I. Virt // *Nukleonika* **58** (2013) 359.
[29] P.G. Baranov, S.G. Orlinskii, C. de Mello Donega and J. Schmidt // *Phys. Stat. Sol. B* **250** (2013) 2137.
[30] J. Chess, G. Alanko, D.A. Tenne, Ch.B. Hanna and A. Punnoose // *J. Appl. Phys.* **113** (2013) 17C302.
[31] F. Acosta-Humanez, R. Cogollo Pitalua and O. Almanza // *J. Magn. Magn. Mater.* **329** (2013) 39.
[32] N.F. Djaja, D.A. Montja and R. Saleh // *Adv. Mat. Phys. Chem*. **3** (2013) 33.
[33] A. Mesaros, C.D. Ghitulica, M. Popa, R. Mereu, A. Popa, T. Petrisor Jr., M. Gabor, A.I. Cadis and B.S. Vasile // *Ceram. Int*. **40** (2014) 2835.
[34] V. Gandhi, R. Ganesan, H.H. Abdulrahman Syedahamed and M. Thaiyan // *J. Phys. Chem. C* **118** (2014) 9715.
[35] S.K. Misra, S.I. Andronenko, S. Srinivasa Rao, J. Chess and A. Punnoose // *J. Magn. Magn. Mater.* **394** (2015) 138.
[36] A. Savoyant, F. Giovannelli, F. Delorme and A. Stepanov // *Semicond. Sci. Tech.* **30** (2015) 075004.
[37] J.J. Beltran, C.A. Barrero and A. Punnoose // *J. Solid State Chem.* **240** (2016) 30.
[38] K. Samanta, P. Bhattacharya, R.S. Katiyar, W. Iwamoto, P.G. Pagliuso and C. Rettori // *Phys. Rev. B* **73** (2006) 245213.
[39] J.H. Kim, H. Kim, D. Kim, Y.E. Ihm and W.K. Choo // *J. Appl. Phys*. **92** (2002) 6066.
[40] J.S. Thakur, G.W. Auner, V.M. Naik, C. Sudakar, P. Kharel, G. Lawes, R. Suryanarayanan and R. Naik // *J. Appl. Phys.* **102** (2007) 093904.
[41] H. Harima // *J. Phys.: Condens. Mat.* **16** (2004) S5653.
[42] J. Park, M.G. Kim, H.M. Jang, S. Ryu and Y.M. Kim // *Appl. Phys. Lett.* **84** (2004) 1338.
[43] T.L. Estle and M. De Wit // *Bull. Am. Phys. Soc.* **6** (1961) 445.
[44] J.E. Stehr, B.K. Meyer and D.M. Hofmann // *Appl. Magn. Reson*. **39** (2010) 137.
[45] L.S. Vlasenko // *Appl. Magn. Reson*. **39** (2010) 103.
[46] D.V. Azamat, D. Dejneka, V.A. Trepakov, L. Jastrabik, M. Fanciulli, V.Y. Ivanov, M. Godlewski, V.I. Sokolov, J. Rosa and A.G. Badalyan // *Phys. Status Solidi-R.* **5** (2011) 138.
[47] W.L. Roth // *J. Phys. Chem. Solids* **25** (1964) 1.
[48] F. Moro, S.V.Y. Tang, F. Tuna and E. Lester // *J. Magn. Magn. Mater.* **348** (2013) 1.
[49] M. Al-Ghoul, H. El-Rassy, T. Coradin and T. Mokalled // *J. Cryst. Growth* **312** (2010) 856.